Electronic Supplementary Information (ESI) for

Optimal structuring nitrogen-doped hybrid-dimensional nanocarbons for high-performance flexible solid-state supercapacitors

Xianyi Cao,[a] Shuai Jia,[b] Wei Huang,[a] Yingying Tang,[a] Jens Øllgaard Duus,[a] Jun Lou,*[b] and Qijin Chi*[a]

[a] *Department of Chemistry, Technical University of Denmark, DK-2800 Kongens Lyngby, Denmark.*
[b] *Department of Materials Science and NanoEngineering, SDU & Rice Joint Center for Carbon Nanomaterials, Rice University, Houston, TX 77005, USA.*
* *Corresponding authors.* E-mails: cq@kemi.dtu.dk; jlou@rice.edu

I. Experimental details

Chemicals and processing equipment

Unless otherwise noted, all chemicals were of analytical grade and used as received without further purification. PVA (molecular weight: 89,000-98,000), ammonia (25 wt. %), melamine, graphite (powder, particle size: < 20 μm) and H_2SO_4 (97 wt. %) were purchased from Sigma-Aldrich. Nitric acid (HNO_3, 65 wt. %) and ethanol (96%, v/v) were purchased from VWR Chemical. Ethylene glycol was purchased from Bie & Berntsen A/S. Graphite oxide (powder, type: SE2430) was purchased from The Sixth Element. CNTs (multi-walled, outer diameter: < 8 nm, inner diameter: 2-5 nm, length: 10-30 μm) were purchased from Cheap Tubes. CBNPs (VXC-72, highly conductive, particle diameter: ~20 nm) were purchased from Cabot. Milli-Q water (resistivity: 18.2 MΩ cm at 25 °C) and high-purity argon was used throughout.

Microwave synthesis was carried out on an Initiator EXP EU microwave synthesizer (Biotage) with a maximum microwave power of 400 W. Ultrasonication was performed on a USC1200TH high-power ultrasonicator (VWR) with an ultrasonic output frequency of 45 kHz and power of 180 W. Centrifugation was carried out on a 5810 R centrifuge (Eppendorf). Freeze-drying was performed on a MAXI-dry lyo freeze dryer (Heto). Polyvinylidene fluoride

(PVDF) membrane disc filters (Pall) with an average pore size of 0.2 μm and a diameter of 47 mm were used in all filtration processes.

Materials characterization

TEM was carried out on a Tecnai G^2 T20 (FEI) operated at an accelerating voltage of 200 kV. 300 mesh copper grids with lacey carbon support films (Ted Pella) were used as TEM specimen supports. AFM was performed on a 5500 AFM system (Agilent Technologies) operated under a tapping mode with mica as specimen substrates. SEM were recorded by a Quanta FEG 200 ESEM (FEI) at an accelerating voltage of 20 kV. An 80 mm^2 X-Max silicon drift detector (Oxford Instruments) with an energy resolution of 124 eV for Mn-Kα at 100,000 counts per second was attached to the SEM system and used for EDX analysis. XRD measurements were carried out on a D8 Advance X-Ray diffractometer (Bruker). XPS analysis was performed on a K-Alpha X-ray photoelectron spectrometer (Thermo Scientific) with Al-Kα (1486.6 eV) as an excitation X-ray source. Raman spectra were recorded with an InVia confocal Raman microscope (Renishaw), equipped with a 633 nm excitation laser. FTIR measurements were performed on an Alpha-P FTIR spectrometer (Bruker) in the range of 4,000-400 cm^{-1} with a resolution of 2 cm^{-1}. UV-Vis spectra were recorded with an 8453 spectrophotometer (Agilent Technologies) using a quartz cuvette (1 cm light path). TGA was performed on a STA 409 PC Luxx Simultaneous thermal analyzer (Netzsch-Gerätebau GmbH) in dry air at a heating rate of 5 °C min^{-1}. The particle size of CBNPs was characterized by a Zetasizer Nano ZS90 nanoparticle size analyzer (Malvern). Nitrogen adsorption-desorption isotherm analysis was carried out on an ASAP 2020 surface area and porosity analyzer (Micromeritics) at -196 °C, whose samples were degassed in vacuum at 200°C for 3 h prior to use. Specific surface area (s_{BET}, m^2 g^{-1}) and total pore volume (V_t, cm^3 g^{-1}) were calculated by Brunauer-Emmett-Teller (BET) and multipoint methods, respectively. Pore size distribution was calculated by Barrett-Joyner-Halenda (BJH) method using the desorption segments of nitrogen adsorption-desorption isotherm curves. Average pore diameter (D_a, nm) was calculated by the following equation:

$$D_a = \frac{4V_t}{10^3 \times S_{BET}} \quad (1)$$

The sheet resistances of different paper electrodes were measured at 25 °C by a four-point probe system (Jandel) consisting of a Multi Height AFPP2 probe combined with a RM3000+ test unit. The cross-plane resistances of different paper electrodes was measured at 25 °C by a U1231A multimeter (Agilent). Mechanical properties of paper electrodes were analyzed by a Microtest 200N tensile tester (Deben). Different paper electrodes were carefully cut into 5 mm × 30 mm test strips, and the tests were conducted at a strain rate of 0.1 mm min^{-1}.

Processing and pretreatment on nanocarbons

Before used for synthesizing N-RGO-CNT-CBNP, both CNTs and CBNPs were activated by oxidation with a mixture of HNO_3 (65 wt. %) and H_2SO_4 (97 wt. %) (v:v=1:3). In a typical process for preparing activated CNTs, CNTs (1 g) were first added into the mixed acid (320 mL). The suspension was refluxed under continuous stirring at 70 °C for 3 h. Then, the obtained mixture was diluted, filtered and washed with water repeatedly until the used water having a pH of 6-7. Finally, the clean and activated CNTs was freeze-dried for 24 h for subsequent use. In a typical process for preparing activated CBNPs, CBNPs (1 g) were first added into the mixed acid (60 mL). The suspension was then sonicated at 70 °C for 12 h. After that, by following the same washing and drying procedures for activated CNTs, activated CBNPs were collected for further use.

The graphene oxide aqueous suspension used for synthesizing N-RGO-CNT-CBNPs was prepared by ultrasonication assisted liquid-phase exfoliation of graphite oxide. Briefly, graphite oxide (1.5 g) and ammonia (25 wt. %, 5 mL) was added into water (200 mL) and ultrasonicated for 4 h. The obtained aqueous suspension was first centrifuged at 500 rpm for 30 min to remove the bottom sediment containing unexfoliated graphite oxide, and then at 12,000 rpm for 30 min to remove the supernatant containing unwanted tiny graphene oxide fragments. This low-speed/high-speed centrifugation cycle was repeated for several times until the supernatant

reaching a pH of 6-7. The left sediment was re-dispersed in water (50 mL). The graphene oxide concentration was calculated by freeze-drying a certain volume of the aqueous suspension and measuring the weight of left graphene oxide. The graphene oxide concentration was finally adjusted to 4 mg mL^{-1}.

Optimization of N-RGO-CNT-CBNP preparation conditions

The supercapacitive performance of N-RGO-CNT-CBNP could be greatly affected by several key reaction parameters, particularly the weight ratio of different reactants as well as the adopted temperature and duration for thermal annealing. By tuning these parameters, different RGO-CNT-CBNP and N-RGO-CNT-CBNP samples were preliminarily prepared with their supercapacitive performances briefly assessed.

A conventional three-electrode set-up was used for this evaluation, which consisted of a glassy carbon electrode (geometric electrode area: 0.07 cm^2) loading with 10 μg of different materials as the working electrode, a coiled platinum wire as the counter electrode, a SCE as the reference electrode, and 1 M H_2SO_4 as the electrolyte. RGO-CNT-CBNP and N-RGO-CNT-CBNP samples synthesized under different reaction conditions were simply evaluated by comparing their mass specific capacitance values obtained from GCD tests.

The weight ratio of three nanocarbons (RGO:CNT:CBNP) was firstly optimized by comparing the mass specific capacitance values of different RGO-CNT-CBNP samples. Eleven samples with different RGO:CNT:CBNP weight ratios (1:1:1, 1:2:1, 1:1:2, 2:1:1, 1:4:1, 1:1:4, 4:1:1, 8:1:1, 2:1:□, 2:□:1, 1:□:□; □ means no addition) were synthesized with all other parameters kept same. Among them, the 4:1:1 sample could achieve the highest capacitance (246 F g^{-1} at 1 A g^{-1}). After that, the impact of adjusting the added amount of melamine on the overall nitrogen content and the mass specific capacitance of N-RGO-CNT-CBNP was further investigated (Fig. S10), by which a weight ratio of melamine to three nanocarbons was optimized to 3.5:1. Besides, we also investigated the impact of adopting different temperatures and duration for thermal annealing. The three tested samples (800 °C and 1 h, i.e., N-RGO-

CNT-CBNP; 800 °C and 3 h, denoted as N-RGO-CNT-CBNP-800-3; 900 °C and 1 h, denoted as N-RGO-CNT-CBNP-900-1) could achieve similar overall N-doping levels, but the supercapacitive performance of N-RGO-CNT-CBNP was slightly higher than those of N-RGO-CNT-CBNP-800-3 and N-RGO-CNT-CBNP-900-1 (Table S3). This phenomenon, which was in accordance with the result observed by Chen's group, could be because the slightly lower percentage of pyridinic and pyridinic oxide nitrogen in N-RGO-CNT-CBNP resulted in a higher electrical conductivity, thus helping achieve a better supercapacitive performance.[20] Besides, by referring to the thermal annealing condition used by Xia's group,[38] a complete decomposition of g-C_3N_4 can be realized after a thermal annealing process of 800 °C and 1 h. Considering also its relatively low energy consumption and short processing period, 800 °C and 1 h was finally adopted in our study.

Based on the above optimization process, the optimal reaction condition we finally adopted could endow the as-synthesized N-RGO-CNT-CBNP with the highest specific capacitance among all the tested samples, which was then further used for fabricating N-RGO-CNT-CBNP-Ps.

Preparation of PVA-H_2SO_4 gel electrolyte

The PVA-H_2SO_4 gel electrolyte was prepared as follows: H_2SO_4 (1 g) was added to water (10 mL), and then PVA (1 g) was added and stirred for 12 h. After that, the mixture was heated to 85 °C under stirring until it became clear. Then the gel electrolyte was cooled down to room temperature for subsequent use.

Fabrication of working electrodes for electrochemical evaluation

N-RGO-CNT-CBNP-P (or G-N-RGO-CNT-CBNP-P, GC-Blank-P) based working electrodes were prepared as follows. A piece of N-RGO-CNT-CBNP-P (or G-N-RGO-CNT-CBNP-P, GC-Blank-P) was cut into several strips (8 mm in length, 5 mm in width). Then, one strip was stuck onto one end of a polyvinyl chloride (PVC) strip (50 mm in length, 5 mm in width, 0.5 mm in thickness) with double-sided adhesive tapes. After that, in order to ensure a highly

conductive connection, a piece of Cu foil conductive adhesive tape (44 mm in length, 4 mm in width) was adhered to the PVC strip with its one end attached onto the N-RGO-CNT-CBNP-P surface. Finally, the working electrode was carefully encapsulated by waterproof insulating polyimide adhesive sealing tapes with a small area of the N-RGO-CNT-CBNP-P (5 mm in length, 5 mm in width) left for exposure to the electrolyte and a small area of copper foil (3 mm in length, 4 mm in width) left as an electrode terminal. Prior to all electrochemical measurements, working electrodes were immersed in electrolyte under vacuum for 12 h. It should be noted that in practical use, our N-RGO-CNT-CBNP-Ps are capable of directly serving as flexible freestanding electrodes. The above-mentioned fabrication process for N-RGO-CNT-CBNP-P (or G-N-RGO-CNT-CBNP-P, GC-Blank-P) based working electrodes aims at laying out a fixed apparent area of the supercapacitive material for electrolyte approaching and further restraining electrolyte creepage during measurements, both of which are very conducive to minimizing systematic experimental errors.

Electrochemical calculations

With regard to the electrochemical evaluation process for the optimization of N-RGO-CNT-CBNP preparation conditions, based on GCD data obtained from the three-electrode tests, mass specific capacitances of different active materials (C_m, F g^{-1}) were calculated by the following equation:

$$C_m = \frac{I(\Delta t)}{m(\Delta V)} \tag{2}$$

where m (g) is the weight of a tested material, I (A) is the applied discharge current, ΔV (V) is the voltage drop during discharge, and Δt (s) is the discharge time.

Based on GCD data obtained from the three-electrode tests, areal specific capacitances of different paper electrodes (C_a, mF cm^{-2}) were calculated by the following equation:

$$C_a = \frac{1000 \times I(\Delta t)}{s(\Delta V)} \tag{3}$$

where s (cm^2) is the apparent active area of a tested paper electrode.

Mass specific capacitances (C_{N3C}, F g^{-1}) of N-RGO-CNT-CBNP were calculated by the following equation:

$$C_{N3C} = \frac{C_{N3CP} - C_{GCP}}{m_{N3C}} = \frac{I(\Delta t_{N3CP} - \Delta t_{GCP})}{m_{N3C}(\Delta V)} \quad (4)$$

where m_{N3C} is the weight (g) of N-RGO-CNT-CBNP in the N-RGO-CNT-CBNP-P based working electrode, C_{N3CP} (or C_{GCP}, F) is the measured capacitance of the N-RGO-CNT-CBNP-P (or GC-Blank-P) based working electrode, and Δt_{N3CP} (or Δt_{GCP}, s) is the corresponding discharge time for the N-RGO-CNT-CBNP-P (or GC-Blank-P) based working electrode. Referring to this, mass specific capacitances of other materials could also be calculated through replacing Δt_{N3CP} by the corresponding discharge time of other electrodes.

Based on GCD data obtained from the two-electrode tests, areal specific capacitances ($C_{a,F}$, mF cm^{-2}) of the N-RGO-CNT-CBNP-P based FSSSC were calculated by the following equation:

$$C_{a,F} = \frac{1000 \times I_F(\Delta t_F)}{s_F(\Delta V_F)} \quad (5)$$

where s_F (cm^2) is the working area of the N-RGO-CNT-CBNP-P based FSSSC, I_F (A) is the applied discharge current, ΔV_F (V) is the voltage drop during discharge, and Δt_F (s) is the discharge time.

Areal specific energy ($E_{a,F}$, mW h cm^{-2}) and areal specific power ($P_{a,F}$, mW cm^{-2}) of the N-RGO-CNT-CBNP-P based FSSSC were calculated by the following equation:

$$E_{a,F} = \frac{1}{2 \times 3600} C_{a,F}(\Delta V_F)^2 \quad (6)$$

$$P_{a,F} = \frac{E_{a,F}}{\Delta t_F} \times 3600 \quad (7)$$

Mass specific energy ($E_{m,F}$, W h kg^{-1}) and mass specific power ($P_{m,F}$, W kg^{-1}) of the N-RGO-CNT-CBNP-P based FSSSC were calculated by the following equation:

$$E_{m,F} = \frac{1000}{2 \times 3600} \frac{C_{a,F} \times s_F}{m_F} (\Delta V_F)^2 \quad (8)$$

$$P_{m,F} = \frac{E_{m,F}}{\Delta t_F} \times 3600 \tag{9}$$

where m_F (mg) is the mass of the N-RGO-CNT-CBNP-P based FSSSC.

II. Supporting data

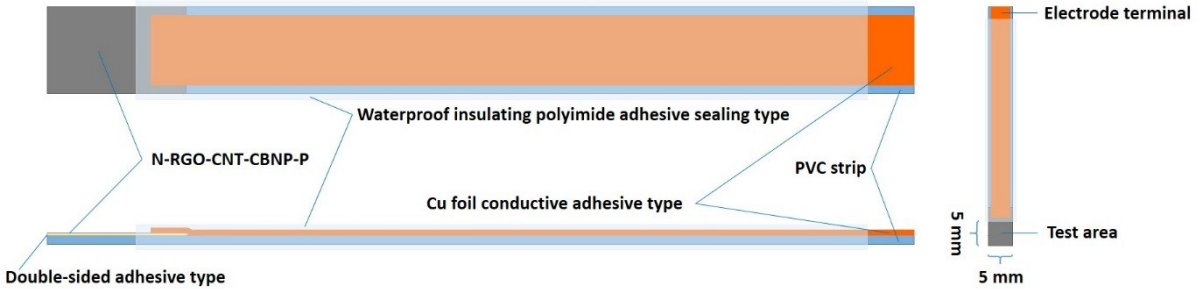

Fig. S1. Schematic of the N-RGO-CNT-CBNP-P based working electrode for electrochemical experiments. Not drawn to scale.

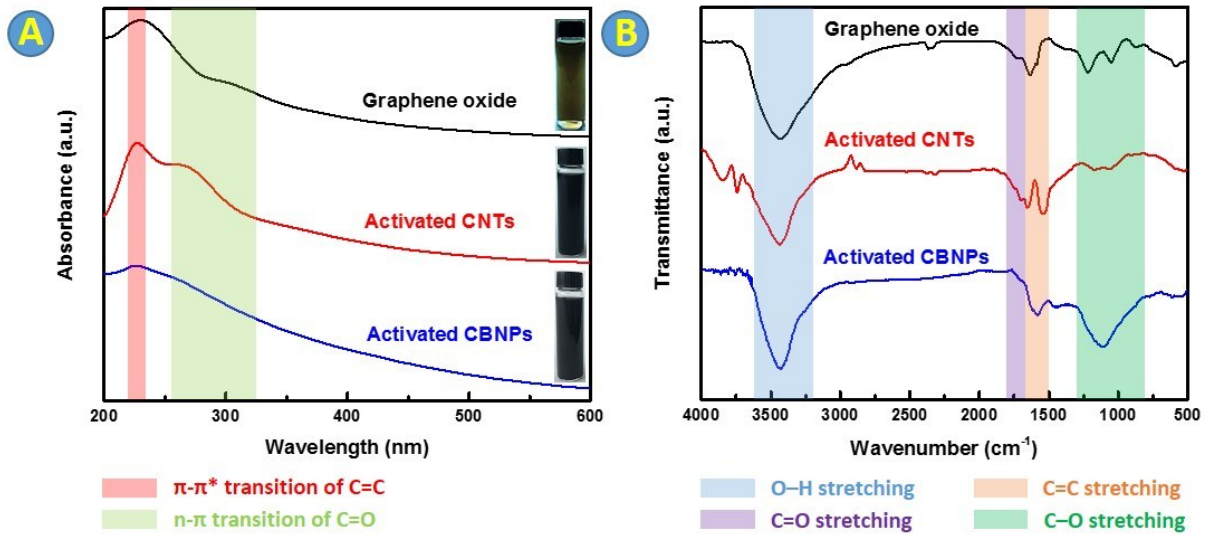

Fig. S2. (A) UV-Vis spectra of aqueous suspensions of graphene oxide, activated CNTs and activated CBNPs. Insets: associated photos of aqueous suspensions of graphene oxide, activated CNTs and activated CBNPs. (B) FTIR spectra of graphene oxide, activated CNTs and activated CBNPs.

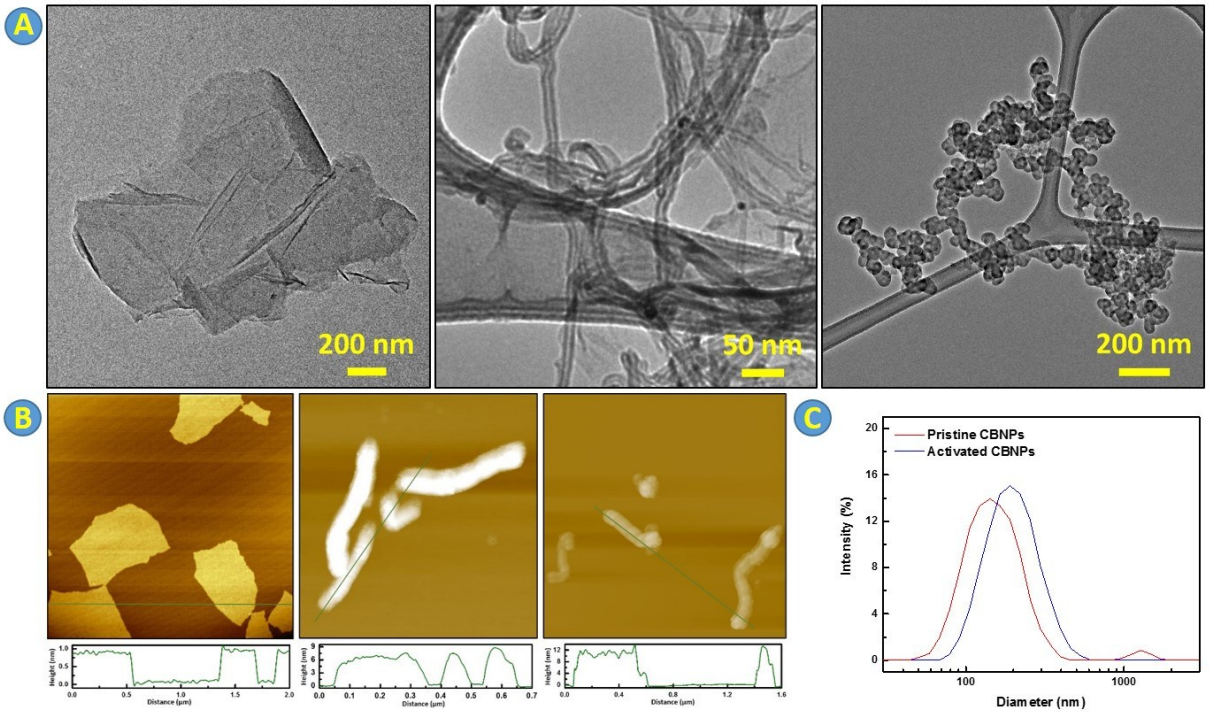

Fig. S3. (A) TEM images of graphene oxide (left), activated CNTs (middle) and activated CBNPs (right). (B) AFM images of graphene oxide, pristine CNTs (middle) and activated CNTs (right). (C) The size distribution of pristine and activated CBNPs measured by DLS. The adopted solvent in DLS samples is a mixture of ethylene glycol and water (v:v=1:2).

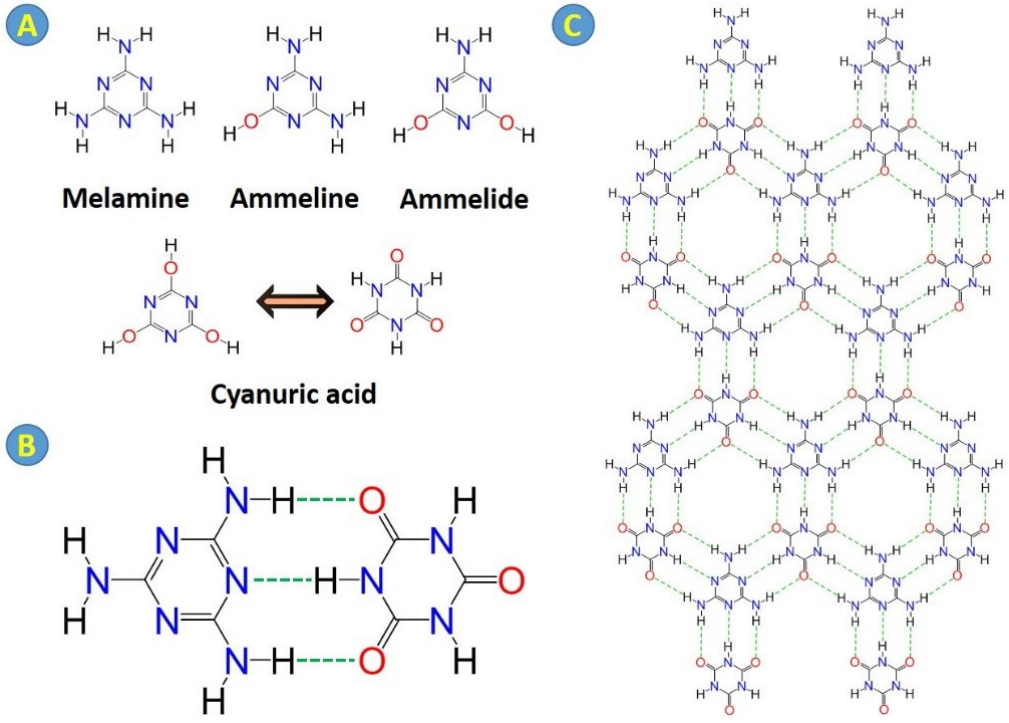

Fig. S4. (A) Schematic of molecular structures of melamine and its primary (ammeline), secondary (ammelide) and tertiary (cyanuric acid) hydrolyzates. Cyanuric acid molecules generally exist in two different structures (tautomers) that can readily interconvert, since the hydrogen atoms of their –OH groups tend to shift positions to form –NH groups. (B) Schematic of the strong hydrogen bonding between individual melamine and cyanuric acid molecules. (C) Schematic of molecular clusters composed of melamine and cyanuric acid molecules.

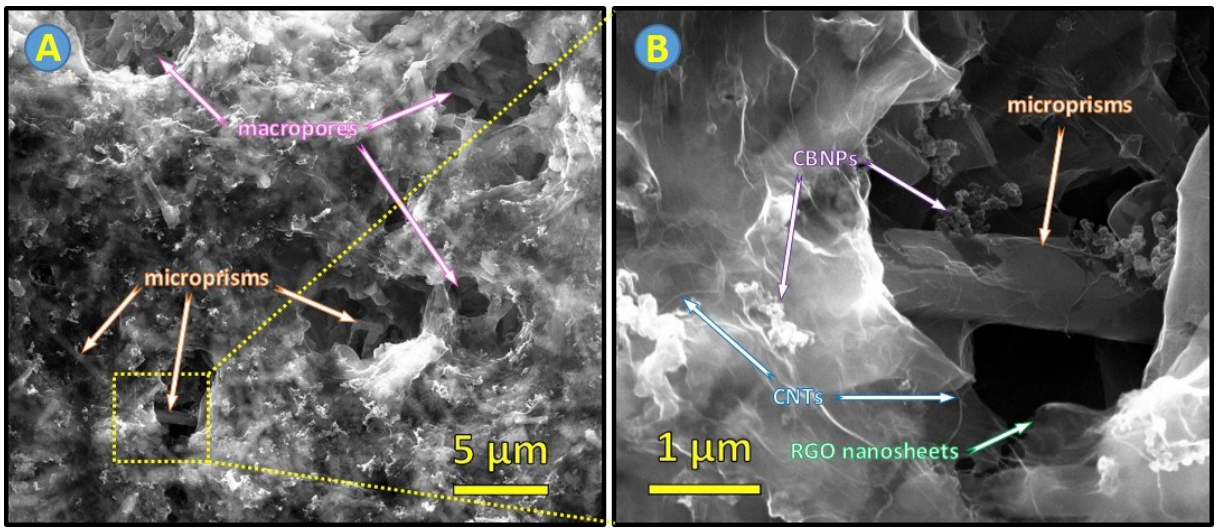

Fig. S5. Low (A) and high (B) magnification SEM images of M-RGO-CNT-CBNP.

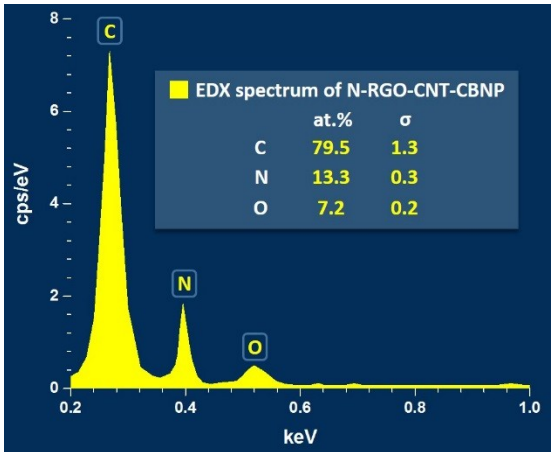

Fig. S6. The EDX spectrum of N-RGO-CNT-CBNP obtained from observing the sample area shown in Figure 7D.

Fig. S7. Photos of an N-RGO-CNT-CBNP-P showing its flexibility: (A) initial state; (B) folded once; (C) folded twice; (D) folded thrice; (E) unfolded completely.

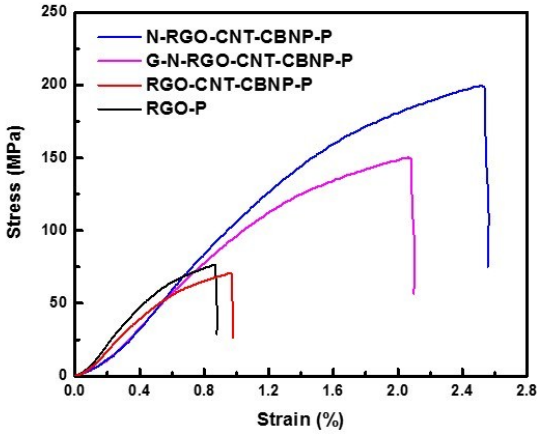

Fig. S8. Stress-strain curves of different paper electrodes.

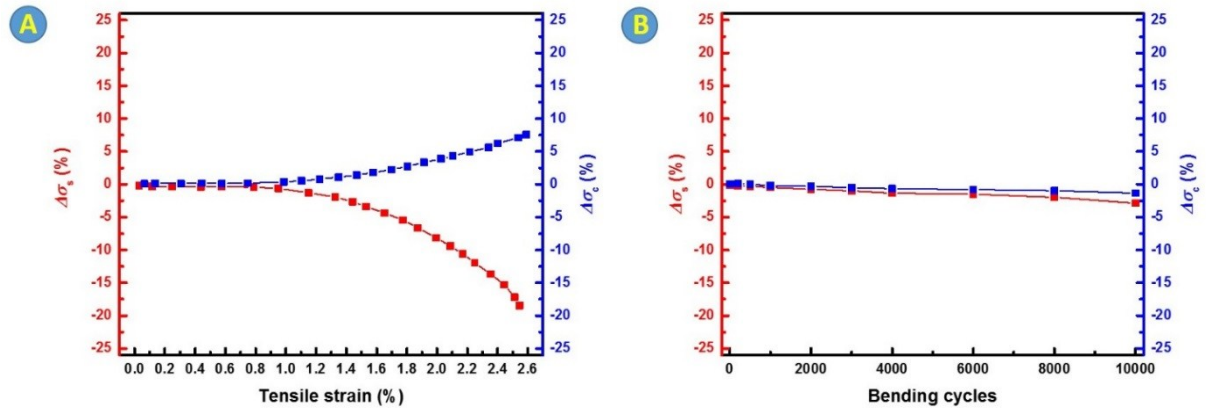

Fig. S9. (A) Curves showing change percentages of surface electrical conductivity ($\Delta\sigma_s$) and cross-plane electrical conductivity ($\Delta\sigma_c$) of an N-RGO-CNT-CBNP-P under increased tensile strain. (B) Curves showing change percentages of surface electrical conductivity ($\Delta\sigma_s$) and cross-plane electrical conductivity ($\Delta\sigma_c$) of an N-RGO-CNT-CBNP-P under repeated bending-unbending cycles with a constant curvature radius of ~4 mm.

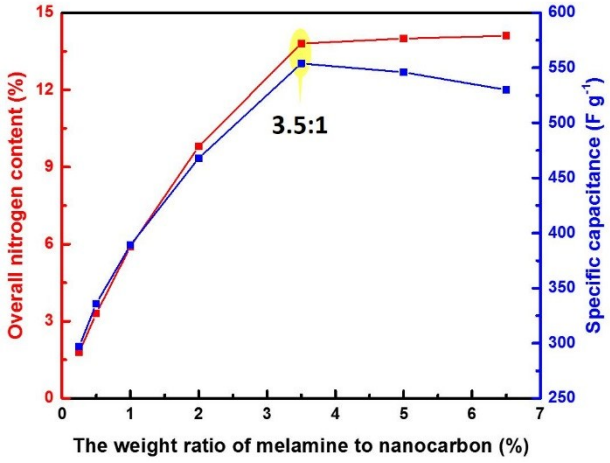

Fig. S10. The impact of regulating the weight ratio of melamine to nanocarbon on the overall nitrogen content and the mass specific capacitance of N-RGO-CNT-CBNP. Electrolyte: 1 M H_2SO_4; Current density: 1 A g^{-1}.

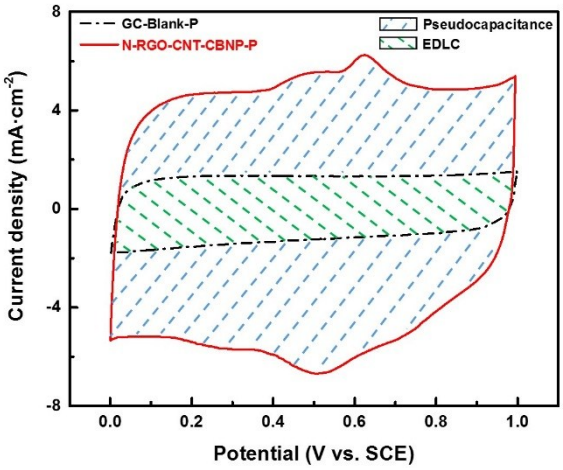

Fig. S11. Schematic showing the calculation principle for the mass specific capacitance of N-RGO-CNT-CBNP.

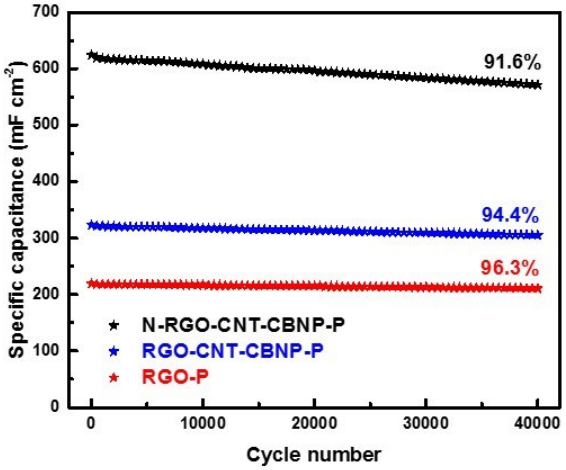

Fig. S12. A comparison on cyclic stability of an N-RGO-CNT-CBNP-P, a RGO-CNT-CBNP-P and a RGO-P at a current density of 50 mA cm^{-2}.

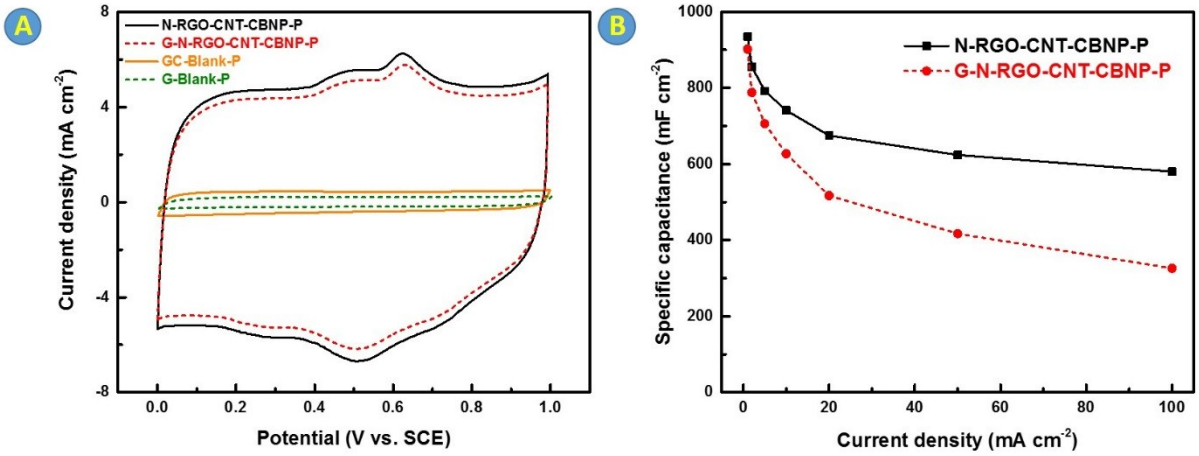

Fig. S13. (A) CV curves of an N-RGO-CNT-CBNP-P, a G-N-RGO-CNT-CBNP-P, a GC-Blank-P and a G-Blank-P at a scan rate of 5 mV s^{-1}. (B) Areal specific capacitances of an N-RGO-CNT-CBNP-P and a G-N-RGO-CNT-CBNP-P at different current densities.

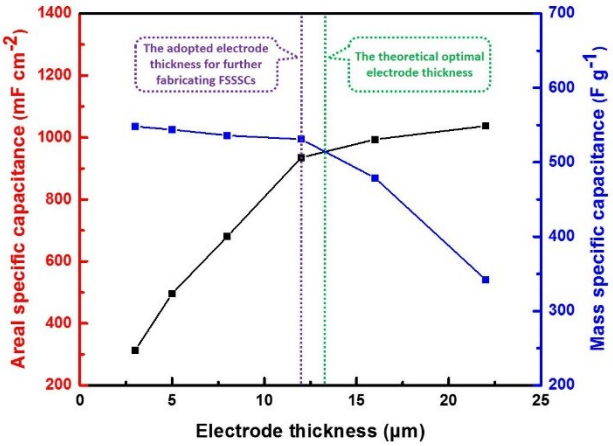

Fig. S14. The impact of regulating the thickness of an N-RGO-CNT-CBNP-P by adjusting the added amount of N-RGO-CNT-CBNP on the areal specific capacitance of the N-RGO-CNT-CBNP-P and the mass specific capacitance of N-RGO-CNT-CBNP. Electrolyte: 1 M H_2SO_4; Current density: 1 mA cm^{-2} (N-RGO-CNT-CBNP-P), 1 A g^{-1} (N-RGO-CNT-CBNP).

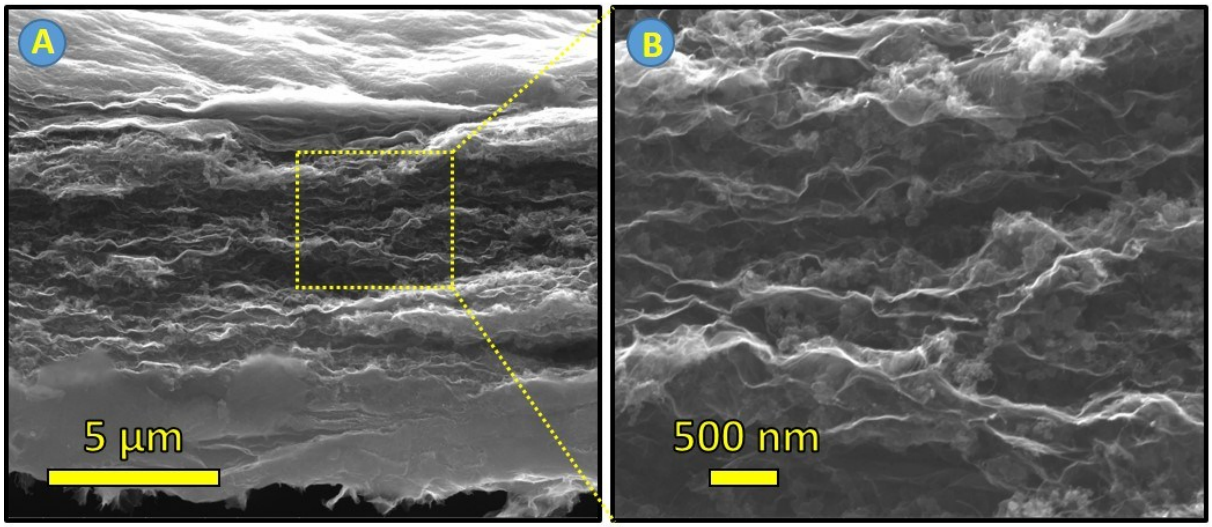

Fig. S15. (A) A cross-sectional SEM photo of an N-RGO-CNT-CBNP-P after 30,000 cycles at a current density of 50 mA cm^{-2} and (B) a high-resolution cross-sectional SEM photo showing the interlayer of the N-RGO-CNT-CBNP-P.

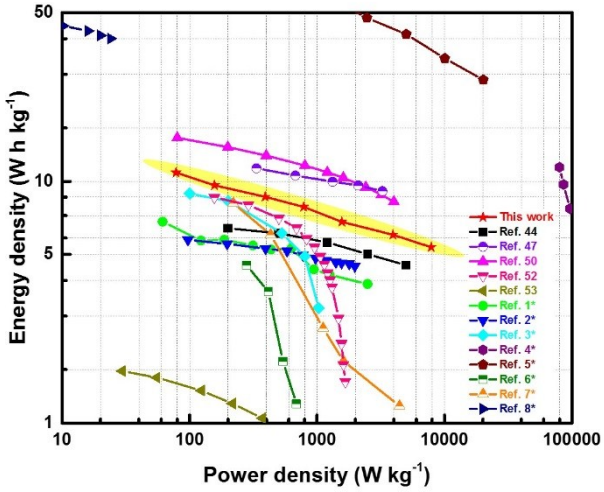

Fig. S16. Gravimetric Ragone plots of the N-RGO-CNT-CBNP-P based FSSSC and some other reported supercapacitor devices. References with a star superscript were listed in the reference list of the supporting information.

Table S1. A comparison on the electrical conductivity of different nanocarbon based papers in this study.

Sample	R_s (Ω sq^{-1})	σ_s (S cm^{-1})	R_c (Ω)	δ (μm)	σ_c (×10^{-6} S cm^{-1})
N-RGO-CNT-CBNP-P	4.7±0.1	1934	74±11	10.8±1.4	1.16
G-N-RGO-CNT-CBNP-P	17.4±0.5	639	156±0.5	10.4±1.2	0.53
RGO-CNT-CBNP-P	-	-	97±0.5	7.4±1.0	0.61
RGO-CNT-P	-	-	176±0.5	6.4±0.7	0.29
RGO-CBNP-P	-	-	305±0.5	6.9±0.8	0.18
RGO-P	-	-	522±0.5	5.9±0.5	0.09
GC-Blank-P	-	-	18±2	2.3±0.2	1.02

Note: 1. R_s: sheet resistance, σ_s: surface electrical conductivity, R_c: cross-plane resistance, δ: the thickness of a paper (observed by SEM), σ_c: cross-plane electrical conductivity. All the measured values in the table are the mean values of ten times' measurements with randomly choosing measured positions.

2. σ_s is calculated by the following equation:

$$\sigma_s = \frac{1}{10^{-4} \times R_s \times \delta_s}$$

where δ_s (μm) is the thickness of a single capping layer. Observed by SEM, the δ_s values of an N-RGO-CNT-CBNP-P and a G-N-RGO-CNT-CBNP-P are 1.1±0.1 and 0.9±0.1 μm, respectively.

3. σ_c is calculated by the following equation:

$$\sigma_c = \frac{1}{\rho_c} = \frac{\delta}{10^4 \times R_c \times S}$$

where ρ_c (Ω cm) is the cross-plane resistivity of a paper, and S (cm^2) is the area of a paper. In our study, the diameters (D, cm) of all paper electrodes are 4 cm, thus S is equal to 12.56 cm^2 according to the formula for circle area:

$$S = \pi(\frac{D}{2})^2$$

Table S2. A comparison on the mechanical performance of different papers in this study.

Sample	Young's modulus (GPa)	Tensile strength (MPa)	Failure strain (%)
N-RGO-CNT-CBNP-P	7.9	200±19	2.56±0.22
G-N-RGO-CNT-CBNP-P	7.3	150±15	2.10±0.15
RGO-CNT-CBNP-P	7.1	71±9	0.98±0.07
RGO-P	8.6	76±5	0.88±0.07

Note: All the measured values in the table are the mean values of five parallel measurements.

Table S3. A comparison on the overall N-doping content and the mass specific capacitance of N-RGO-CNT-CBNP synthesized under different temperatures and durations.

Samples	Overall N (%)	Pyridinic N (%)	Pyrrolic N (%)	Graphitic N (%)	Pyridinic oxide N (%)	Mass specific capacitance (F g^{-1})
N-RGO-CNT-CBNP	13.8	41.5	46.3	4.2	8.0	554
N-RGO-CNT-CBNP-800-3	13.6	43.3	45.8	4.2	6.7	541
N-RGO-CNT-CBNP-900-1	13.9	46.4	45.2	4.3	4.1	548

Table S4. A comparison on the areal specific capacitance of different flexible electrodes in this study and some recent reports. References with a star superscript were listed in the reference list of the supporting information.

Material	Scan rate/ current density	Areal specific capacitance (mF cm^{-2})	Ref.
3D graphene hydrogel film	1 A g^{-1}	372[#]	44
Graphene-CNT hybrid film	1 mA cm^{-2}	33	45
Patterned graphene-CNT loaded on poly(ethylene terephthalate) film	1 mA cm^{-2}	2.54[#]	46
N-doped carbon coated on carbon cloth	5 mV s^{-1}	704.5	47
MnO_2 grown on carbon nanofiber paper	3 mA cm^{-2}	525	48
Graphene/activated carbon/polypyrrole film	0.5 mA cm^{-2}	906	49
3D graphene oxide/polypyrrole loaded on Titanium foil	0.2 mA cm^{-2}	387.6	50
GC-Blank-P	1 mA cm^{-2}	90	This work
RGO-P	1 mA cm^{-2}	286	This work
RGO-CBNP-P	1 mA cm^{-2}	316	This work
RGO-CNT-P	1 mA cm^{-2}	369	This work
RGO-CNT-CBNP-P	1 mA cm^{-2}	445	This work
N-RGO-CNT-CBNP-P	1 mA cm^{-2}	935	This work

Note: [#] Values of full supercapacitor devices.

Table S5. A comparison on the supercapacitive performances of various heteroatom-doped graphene based nanocarbon composites reported by this study as well as some papers in the period of 2016-2018. References with a star superscript were listed in the reference list of the supporting information.

Material	Scan rate/ current density	Mass specific capacitance (F g^{-1})	Cyclic performance	Ref.
S,N-doped RGO	0.5 A g^{-1}	264.3	95% retention, 5,000 cycles, 5 A g^{-1}	9*
S-doped RGO	0.04 A g^{-1}	392	91% retention, 2,000 cycles, 2.4 A g^{-1}	10*
N-doped graphene 3D aerogel	1 A g^{-1}	345.8	92% retention, 2,000 cycles, 1 A g^{-1}	11*
N-doped graphene aerogel	1 A g^{-1}	290	90% retention, 2,000 cycles, 1 A g^{-1}	12*
S,N-doped graphene aerogel	1 A g^{-1}	203.2	90% retention, 3,000 cycles, 2 A g^{-1}	13*
N-doped RGO	1 A g^{-1}	390	97% retention, 20,000 cycles, 10 A g^{-1}	14*
3D N-doped graphene	1 A g^{-1}	408	91% retention, 5,000 cycles, 1 A g^{-1}	15*
N-doped activated carbon/graphene	1 A g^{-1}	512	113.5% retention, 6,000 cycles, 1 A g^{-1}	16*
N-doped RGO/CNT	1 A g^{-1}	142	76% retention, 1,000 cycles, 1 A g^{-1}	17*
N-doped graphene/carbon nanohorn	1 A g^{-1}	363	94% retention, 5,000 cycles, 100 mV s^{-1}	18*
Graphene hydrogel/N,O-doped carbon dots	1 A g^{-1}	335	83% retention, 10,000 cycles, 5 A g^{-1}	19*
N-doped carbon nanosphere encapsulated graphene	1 A g^{-1}	242	95% retention, 10,000 cycles, 5 A g^{-1}	20*
N-doped RGO	1 A g^{-1}	230	88% retention, 10,000 cycles, 5 A g^{-1}	21*
N-RGO-CNT-CBNP	1 mA cm^{-2} (~0.4 A g^{-1})	531	91.6% retention, 40,000 cycles, 50 mA cm^{-2} (~21 A g^{-1})	This work

References

[1] Y. He, W. Chen, X. Li, Z. Zhang, J. Fu, C. Zhao and E. Xie, *ACS Nano*, 2013, **7**, 174-182.

[2] H. Inoue, Y. Namba and E. Higuchi, *J. Power Sources*, 2010, **195**, 6239-6244.

[3] Y. Cheng, S. Lu, H. Zhang, C. V. Varanasi and J. Liu, *Nano Lett.*, 2012, **12**, 4206-4211.

[4] G. Yu, L. Hu, M. Vosgueritchian, H. Wang, X. Xie, J. R. McDonough, X. Cui, Y. Cui and Z. Bao, *Nano Lett.*, 2011, **11**, 2905-2911.

[5] Q. Liao, N. Li, S. Jin, G. Yang and C. Wang, *ACS Nano*, 2015, **9**, 5310-5317.

[6] S. S. Raut and B. R. Sankapal, *Electrochim. Acta*, 2016, **198**, 203-211.

[7] S. Nagamuthu, S. Vijayakumar and G. Muralidharan, *Dalton Trans.*, 2014, **43**, 17528-17538.

[8] B. G. Choi, M. Yang, W. H. Hong, J. W. Choi and Y. S. Huh, *ACS Nano*, 2012, **6**, 4020-4028.

[9] P. Tian, J. Zang, S. Jia, Y. Zhang, H. Gao, S. Zhou, W, Wang, H. Xu and Y. Wang, *Appl. Surf. Sci.*, 2018, **456**, 781-788.

[10] M. Duraivel, S. Nagappan, B. Balamuralitharan, S. Selvam, S. N. Karthick, K. Prabakar, C. S. Ha and H. J. Kim, *New J. Chem.*, 2018, **42**, 11093-11101.

[11] X. L. Su, M. Y. Cheng, L. Fu, G. P. Zheng, X. C. Zheng, J. H. Yang and X. X. Guan, *New J. Chem.*, 2017, **41**, 5291-5296.

[12] X. L. Su, L. Fu, M. Y. Cheng, J. H. Yang, X. X. Guan and X. C. Zheng, *Appl. Surf. Sci.*, 2017, **426**, 924-932.

[13] Y. Chen, Z. Liu, L. Sun, Z. Lu and K. Zhuo, *J. Power Sources*, 2018, **390**, 215-223.

[14] S. Dai, Z. Liu, B. Zhao, J. Zeng, H. Hu, Q. Zhang, D. Chen, C. Qu, D. Dang and M. Liu, *J. Power Sources*, 2018, **387**, 43-48.

[15] B. Wang, Y. Qin, W. Tan, Y. Tao and Y. Kong, *Electrochim. Acta*, 2017, **241**, 1-9.

[16] Z. Gao, X. Liu, J. Chang, D. Wu, F. Xu, L. Zhang, W. Du and K. Jiang, *J. Power Sources*, 2017, **337**, 25-35.

[17] F. Y. Ban, S. Jayabal, H. N. Lim, H. W. Lee and N. M. Huang, *Ceram. Int.*, 2017, **43**, 20-27.

[18] X. Q. Lin, W. D. Wang, Q. F. Lv, Y. Q., Jin, Q. Lin and R. Liu, *J. Mater. Sci. Technol.*, 2017, **33**, 1339-1345.

[19] L. Xu, X. Dun, J. Zou, Y. Li, M. Jia, L. Cui, J. Gao and X. Jin, *J. Electrochem. Soc.*, 2018, **165**, A2217-A2224.

[20] M. Zhao, X. Cui, Y. Xu, L. Chen, Z. He, S. Yang and Y. Wang, *Nanoscale*, 2018, **10**, 15379-15386.

[21] S. K. Singh, V. M. Dhavale, R. Boukherroub, S. Kurungot and S. Szunerits, *Appl. Mater. Today*, 2017, **8**, 141-149.